Nanocytometer for smart analysis of peripheral blood and acute myeloid leukemia: a pilot study

Schütt, J.; Sandoval Bojorquez, D. I.; Avitabile, E.; Oliveros Mata, E. S.; Milyukov, G.; Colditz, J.; Delogu, L. G.; Rauner, M.; Feldmann, A.; Koristka, S.; Middeke, J. M.; Sockel, K.; Faßbender, J.; Bachmann, M.; Bornhäuser, M.; Cuniberti, G.; Baraban, L.;

Originally published:

August 2020

Nano Letters 20(2020)9, 6572-6581

DOI: https://doi.org/10.1021/acs.nanolett.0c02300

Nanocytometer for smart analysis of peripheral blood and acute myeloid leukemia: a pilot study

Julian Schütt[1,10], Diana Isabel Sandoval Bojorquez[2], Elisabetta Avitabile[3], Eduardo Sergio Oliveros Mata[1,10], Gleb Milyukov[4], Juliane Colditz[7], Lucia Gemma Delogu[3,5], Martina Rauner[7], Anja Feldmann[2], Stephanie Koristka[2]; Jan Moritz Middeke[6], Katja Sockel[6], Jürgen Fassbender[10], Michael Bachmann[2], Martin Bornhäuser[6], Gianaurelio Cuniberti[1,8,9*], and Larysa Baraban[1,2,8*]

[1] Max Bergmann Center of Biomaterials and Institute for Materials Science, Dresden University of Technology, Budapesterstrasse 27, 01069 Dresden, Germany

[2] Helmholtz-Zentrum Dresden-Rossendorf e.V., Institute of Radiopharmaceutical Cancer Research, Bautzner Landstrasse 400, 01328 Dresden, Germany

[3] Department of Chemistry and Pharmacy University of Sassari, via muroni 23, 07100 Sassari, Italy

[4] Samsung R&D Institute Russia, Moscow, Samsung R&D Institute Russia (SRR), Moscow, Russia

[5] Department of Biomedical Sciences, University of Padua, via Ugo bassi 58, Italy

[6] Medizinische Klinik und Poliklinik I, Universitätsklinikum Carl Gustav Carus Dresden, Dresden

[7] Medizinische Klinik und Poliklinik III, Universitätsklinikum Carl Gustav Carus Dresden, Dresden

[8] Center for Advancing Electronics Dresden (cfaed), Technische Universität Dresden, 01069 Dresden, Germany

[9] Dresden Center for Computational Materials Science (DCMS), TU Dresden, 01062 Dresden, Germany

[10] Helmholtz-Zentrum Dresden-Rossendorf e.V., Institute of Ion Beam Physics and Materials Research, Bautzner Landstrasse 400, 01328 Dresden, Germany

Corresponding authors: l.baraban@hzdr.de, gianaurelio.cuniberti@tu-dresden.de

Abstract: We realize an ultra-compact nanocytometer for real-time impedimetric detection and classification of subpopulations of living cells. Nanoscopic nanowires in a microfluidic channel act as nanocapacitors and measure in real time the change of the amplitude and phase of the output voltage and, thus, the electrical properties of living cells. We perform the cell classification in the human peripheral blood (PBMC), and demonstrate for the first time the possibility to discriminate monocytes and *subpopulations* of lymphocytes in a label-free format. Further, we demonstrate that the PBMC of acute myeloid leukemia and healthy samples grant the label free identification of the disease. Using the algorithm based on machine learning, we generated *specific data patterns* to discriminate healthy donors and leukemia patients. Such solution has the potential to improve the traditional diagnostics approaches with respect to the overall cost and time effort, in a label free format, and restrictions of the complex data analysis.

Keywords: impedance cytometer, nanosensor, POC diagnostics, PBMCs, acute myeloid leukemia (AML), machine learning for data treatment

Healthcare of tomorrow will be dramatically affected by global processes that take place today, like societal shifts[1], technological and digital revolution[2,3]. One of the main challenges within the healthcare sector is to establish new patient-care standards, based on *e.g.* new drug administering[4], novel ultrasensitive diagnostics integrated into the gadgets[5], to provide maximally personalized tests and doctor advices[6]. Medical data for patients will double every 73 days by 2020[7]. Taking into account the trends towards personalization in medicine, patient related data can reach millions of gigabytes during the lifetime[8]. To make this information serving its aim to improve the quality of care while controlling the costs, these data have to be analyzed using *conventional* and *unconventional algorithms*, involving elements of machine learning. This strategy helps to fully access and interpret information on demand using *e.g.* modern gadgets, connected to a cloud. Thus, artificial intelligence is now rapidly entering the medical sector. Ideal proof of concept realization of diagnostic devices combining the new technological trends with the novel data treatment protocols would be a nanoscaled sensor device, for *e.g.* cancer diagnostics, accompanied with algorithms involving machine learning elements to distinguish proper trends within the large amount of noisy data points. The development of such systems is currently in the emerging phase[9,10], due to the number of existing technological challenges, *e.g.* reaching the stable performance of nanosensors as well as its current disintegration with the IT sector.

The primary goal of the current work is to show that all prerequisites for the development of a *nanobiosensor system combined* with a *smart analysitical algorithm* to interpret the results can be achieved.

Leukemia is one of the common forms of blood cancer, affecting the production of white blood cells[11], diagnosed in 352,000 people and caused 256,000 deaths worldwide in 2014[12]. Acute myeloid leukemia (AML) is the most frequent type in adults, with around 30% of all detected leukemia cases and relatively low five-year survival rate of 20-30%, strongly dependent on the age of the patient[13,14]. Diagnosis of AML is multidimensional[15-19], including examination of blood by flow cytometry. More specifically, optical flow cytometry makes a big impact in blood cancer diagnostics[20,21] and evaluation of the immune response of the patient[22,23] via analysis of peripheral blood mononuclear cells (PBMCs)[24–26]. For a complete qualitative and quantitative detection of blood cancer[26] in PBMCs, the main immune cell subpopulations have to be distinguished, exploiting the *clusters of differentiation* (CD) responsible for cell surface marker expressions. Conventional flow cytometers rely on the use of specific molecular labels, *e.g.* monoclonal antibodies against cell surface markers[27]. Finally, a combination of this and above mentioned techniques rises the diagnostics costs of cancer up to hundreds of dollars per person[28].

On-chip integrated nanodevices have emerged as a new generation of biodetectors [29-38]. A promising approach relies on measuring electrical signals, *e.g.* impedance. For the latter, *static* (electrical impedance spectroscopy (EIS)[39-43]) and *dynamic* (impedance cytometry[44–47]) modes of impedance detection are proposed. The latter one is performed at fixed frequency and is used to increase an analytic and information processing throughput. From the conceptual introduction of micro-Coulter counters[44,48], impedance cytometry has evolved and strengthened its impact in biological contexts for single cell detection[45,46], investigations of erythrocytes[49,50], eukaryotes[51,52] and protozoa[53] (Figure 1 A).

The scientific community accepts that scaling down of the sensor dimensions boosts the sensitivity of common detection techniques. Despite the tremendous success of *e.g.* nanoscaled bio-FETs[54], the sensitivity issue of impedance detectors and its possible improvement via cross-scale integration of the nanostructures, have not yet been addressed. All current realizations of impedance dynamic sensors are characterized by macro- to micro-dimensions, employing metal microscopic electrodes in a fluidic channel[49,50,55,56]. Proof-of-concept realizations of such devices are limited to detection of inorganic particles and isolated and purified/treated eukaryotic cells[56–58] with very few examples demonstrating the realistic systems, *e.g.* purified or diluted blood[59], typically used for clinical diagnostics.

Here, we present a nanosensor system, combining an ultra-compact impedance flow cytometer to analyze complex cell compositions with a software, based on conventional machine-learning algorithms, to interpret the measured data via exploiting the classification of cell subpopulations and respective clusters of differentiation (see Figure 1 B). Utilizing the term "nanocytometer"[60], we work with a nanosensor that employs the interdigitated pairs of gold nanoelectrodes to reach the substantial increase of the sensitivity[36,61], compared to the micron structures. We study untreated human PBMCs from healthy volunteers (Figure 1, C and D) and AML patients, and demonstrate significant differences in data patterns of healthy PBMC and AML samples (see Table S1 in **Supporting**). Thanks to the enhanced sensitivity of the device, we show the discrimination of the cells subpopulations in a label free format, *e.g.* B-, T, NK cells and myeloblasts that before was possible only using fluorescent biomarkers. The software processes the output voltage and phase signals measured by the detector in a multistep manner, followed by a final data clustering using the k-means algorithm.Fabrication of gold nanowire arrays is summarized in Figure 2, A.I-III and C, and detailed in **Materials and Methods in Supporting Information.** The resulting cytometer devices possess 1 (sensor area ~46 µm²), 6 (~506 µm²) and 18 pairs of gold nanowires (~1610 µm², see calculations in **Supplementary Information)** with the width of about 100 nm each. To optimize the sensor geometry, COMSOL simulations were carried out to reach the situation of a homogeneous electric field between the nanowires. This electric field is also enhanced (**Supporting Information S1-S3**), compared to the geometry without nanowires. The optimal nanowire configuration was found at a distance of 2 µm from the nanowire tips to the opposing microelectrode pad, with a pitch about 1 µm (Figure 2 B, and **Supporting Information S2**). In order to demonstrate the effect of a 2µm silica particle on the spatial distribution of the electric field and its enhancement near the nanowires, simulations were carried out in *yz*- and *xz*-planes. (Figure 2 B (*yz*-plane) and **Supporting Information S4**). Detailed comparison of the geometry and sensitivity characteristics of the nanocytometer with reported impedance sensor devices is provided in the Table S2 in **Supporting information**.

Next, a PDMS-based 3D flow-focusing system (Figure 2 C), confining the analyte in the middle and bottom of the channel (height 15 µm, width 200 µm) close to the sensor (Figure 2 D, **Supporting Figure S5** for efficiency of the hydrodynamic focusing), was realized. Measurements were carried out with a lock-in amplifier (eLockIn205/2, Anfatec) for a direct readout of the signal. Flow rates were actively manipulated (0.1 µl/min – 2.5 µl/min) using a syringe pump (neMESYS 290N, Cetoni) for injecting a sample solution (particles and cells solution, as well as

vertical and lateral focusing streams (100 µM, KCl). The chip was measured under the microscope (Axiovert200, Carl Zeiss Microscopy) for complementary observations. With respect to the following analysis of *e.g.* peripheral blood, measurements were typically performed with the average cell rate of around 3-5 cells/s at 0.5 µl/min (**see Supporting information S6**). The electrical characterization was carried out in both direct (DC) and alternating current (AC) modes to evaluate the equivalent circuit of the system and is summarized in **Supporting Information S7** and **S8**. The sensing device (*e.g.* 18 NW) exhibits a capacitive behavior with a characteristic butterfly shape in DC voltammetry (**Supporting Information S7**), also confirmed by a Nyquist diagram. Living cells, that cross the sensing area, cause a local alteration of the dielectric properties of the medium around the nanocapacitor, causing an instantaneous modulation of the equivalent circuit and its complex impedance.

Next, we compare three above fabricated nanocytometers to the reference nanowire-free microelectrodes (distance between microelectrodes - 50 µm, width of pads - 35 µm) to investigate the enhancement of the sensitivity and the signal dispersion, depending on the sensor dimensions. We used silica colloidal particles and peripheral blood samples as reference objects. First, a single 10 µm bead was placed onto the sensing area of all types of devices by micropipetting to investigate the EIS signature between 50 Hz and 20 MHz. Dielectric particles deform the semi-circle in the Nyquist diagram (Figure 3, A-B) via adding a particle related *serial RC-element* (accounting for the particles resistance and capacitance), connected in parallel to the initial RC-circuit. Based on Maxwell model for dielectric mixtures, the effect of particles and cells on the impedance signal is described using single shell models. Considering RC-like properties of the sensor, a particle or cell adds its capacitances and resistances of the membrane and cytosol. In the simplified model, cell membrane conductance and cytosol capacitance are ignored, resulting in a parallel addition to the RC-circuit of an in-series cytosol resistance and membrane capacitance[62]. We observe that devices with nanofabricated electrodes, possessing a single pair of nanowires, revealed stronger modulation of the amplitude and phase signals than both multiwire and microelectrode-based sensors (factor of 23 for microelectrode geometry) (see Figure 3 A and B). Thus, enhancement of the electric field between the nanowires boosts the sensitivity of devices towards micro-objects, *e.g.* colloids and living cells. This statement is confirmed by cytometer-like measurements of 10 µm large silica particles in 0.1x phosphate buffered saline (PBS), performed at 100 kHz using devices with 1, 6 and 18 nanowire pairs (Figure 3 C, D). Here, the solution of particles is injected into a microchannel, focused by streams of 100 µM KCl and guided towards the sensors. In the following, the change of the amplitude ΔV_{out} and the phase ΔPhase of the output signal compared to the background, when a particle (or cell) is crossing the active area of the sensor, is evaluated for each detection event. The results are presented as clusters, depicting ΔPhase (*y* axis) versus the ΔV_{out} (*x* axis) of the output signal (**Supporting Information S9-S11** for details). Such representation of detection events allows us to compare not only output *signal modulations* but also the *dispersion* of the signal, measured by different devices. The devices with the smallest area reveal highest signal deviation, but they are prone to higher signal dispersion due to the stronger influence of the spatial location of the particle with respect to the electrodes (Figure 3, D). The sensitivity of the

device in arbitrary units and with respect to *resistance and capacitance changes per particle* is calculated for different sensor dimensions (**Supporting Table S2 and S12-S13)**.

This result is a direct *fundamental consequence of the nanoscopic scaling effect* that makes a great impact in the field of nanobiosensorics. Indeed, the miniaturization of the detector size down to the dimensions of the analyte, boosts its sensitivity on one hand[62], but unavoidably leads to an increase of the signal to noise ratio. We further apply a nanoscaled cytometer with 6 pairs of interdigitated nanowire electrodes for analysis of blood and diagnostics of AML by identifying human PBMC subpopulations with particular interest to classify the subpopulations of the cells within PBMCs in label-free format (*e.g.* monocytes, T-cells, B-cells, NK-cells[63,64], myeloblasts). PBMCs of healthy donors are represented by subpopulations of peripheral cellular blood components exhibiting a round nucleus and visible granules[65], consisting of monocytes (CD14) and lymphocytes which can be additionally divided into T cells ($CD3^+$), B cells (CD19/CD20) and natural killer (NK) (CD16/CD56) cells[63]. In turn, the peripheral blood smear from the AML patients is highly probed with undifferentiated myeloid progenitor cells, the myeloblasts ($CD34^+$/CD123).

First, we realize the measurements of PBMCs in order to determine the specific *calibration pattern*, peculiar for the impedance nanocytometer. The fresh human blood from healthy male donor and AML patient was purified using standardized Ficoll protocol (ratio 1:1) and resuspended in PBS buffer for measurements. This unified protocol has been applied to all further measurements, including impedance and conventional cytometry. Further, the traditional FACS technique was employed to sort the labeled subpopulations of PBMCs into separate vials (*i.e.* monocytes, B-, T-, NK- cells for healthy donor, and myeloblasts for AML positive patient) for *calibration* measurements **(Supporting Information S14**). The output potential ΔV_{out} and phase shift ΔPhase were acquired by applying a sinusoidal reference signal with an amplitude of 0.5 V and a frequency 500 kHz.

Next, we placed the microfluidic chip under the fluorescent microscope to perform parallel impedimetric and microscopy measurements. We did the calibration for healthy samples injecting each cells subpopulations one-by-one (1 - T-cells, 2 - NK cells, 3 – B cells, 4 - Monocytes), and *repeated them in random order sequence* (see 5 - NK-cells, 6 - T-cells, 7 – B-cells, respectively), to prove the fact of the signal differentiation and absence of drift in the system (Figure 4 A, different colors for coding each cell subpopulation). This data sequence resulted in the clusters of differentiations for each of the detected subpopulations (Figure 4, B-G). Measurements of myeloblasts are performed in similar manner and are summarized in Figure 4 L-N. Resulting cloud of the myeloblasts data is plotted in Figure 4 M (red circles) and converged with the whole data pattern of labeled PBMC of the AML patient (black circles) measured by the nanocytometer for localization of the subpopulation of malignant cells. Analysis of the whole datasets determines a *calibration pattern* (Figure 4 H - healthy and M, N - AML, **Supporting S15**). Afterwards, both *labeled* and *unlabeled* PBMC mixtures of a healthy volunteer (Figure 4 J and K, respectively) and AML patient #2 (Figure 4 M and N) were matched to compare with the aforementioned *calibrations* to fine-tune the thresholds for data clustering. Raw samples and calibration patterns match well at the level of the pattern shape, while normalization is needed to compare between labeled/unlabeled samples (**Supporting S16**). Normalization of

the AML data plot in the range [0, 1] enables to match the data patterns of myeloblasts (red circles), unlabeled samples of AML (black circles) and healthy PBMC (green circles, Figure 4 N). Interestingly, analysis of healthy PBMC (green) and myeloblasts (red) shows *additivity* of both patterns. Thus, we believe that the isolated labeled PBMC subpopulations of healthy and AML positive patients can serve as a valid guideline for impedimetric measurements of unlabeled PBMC samples.

Note that the discrimination between PBMC cells according to their dielectric properties has been predicted around two decades ago[66,67]. Natural reason is that the membrane surface of immune cells is not even, and its textures is related to the cells function[68-70]). Still, discrimination of *unlabeled lymphocytes at single cell level* was not demonstrated by now. We attribute successful discrimination of the lymphocyte cells in this work to the essentially increased sensitivity of the nanoscopic cytometer device (**Table S2,** PBMC measured by different sensors in **Supporting Information S16**).

Next, we strengthen the classification of the PBMCs by proportion analysis of all measured cells. All together 5 samples from healthy volunteers were studied (4 male and 1 female, age 25-35 years, **Supporting Table S1**). Calibration patterns are used for determination of the clusters of monocytes and subpopulations of the lymphocytes within the solution (Figure 4 H-K, Figure 5 A (inset), F, and **Supporting Figures S16, S17**). Thus, the subpopulations of T cells (62.31%, purple), B cells (31.34%, green) and NK cells (7.34%, red) could be distinguished (Figure 5 A, inset). These percentages are in agreement with the proportions of cells within healthy human PBMCs predetermined via FACS (**Supporting Information S17**), deviating within 1-3% only (table in Figure 5 D).

Finally, for analysis of AML positive cases, all together 3 patients (2x female, 1x male) were tested, using a small sample volumes, compared to regular assays in the clinical practice[71,72] (~5 µl). Blood from AML Patient#1 (female) and a healthy donor (female) was taken at the same day for comparison (Figure 5 A, and inset in A). Further, 2 samples were analyzed additionally (**Supporting Figure S14** for FACS). Sensors with 18 pairs of nanowires (AML Patient #1) and 6 pairs (AML Patient #2 and #3) were utilized for these studies. All AML data were analyzed manually and compared to the calibration (Figure 4M) and healthy reference, measured earlier. An additional large data cluster was identified in all samples (black circles, Figure 5 A). We attribute it to the myeloblasts that account for 34.16% (AML #1), 60,07% (AML #2) and 54,96% (AML #3) (Figure 5 D, and **Supporting Information S18, S19).** Results are in agreement with the proportions of myeloblasts cells, provided by flow cytometer analysis (**Supporting Information S14,**) and are comparable to the data provided by World Health Organization (WHO)[75]. Further details on cell proportions and merged AML#2-AML#3 data are given in **Supporting S18.**

AML#1 raw data were additionally analyzed with the developed software for classification of cell subpopulations for comparison[73,74]. Algorithm for clustering of the of PBMC cells was divided into four subparts: signals baseline estimation, baseline subtraction, interquartile range analysis for peak detection and coupled peaks clusterization.

(**Supporting Information**, **Methods**). Additional data cluster in the scatter analysis was identified with excellent precision, which can assist in the *pattern based disease diagnostics* (see Figure 5, B-C).

In conclusion, we demonstrate an ultra-compact impedance flow nanocytometer combined with software employing the conventional machine-learning algorithms. We successfully apply this system for the discriminative analysis of healthy PBMC (B-, T-, NK-cells and monocytes), as well as discrimination of PBMCs of leukemia patients, using extremely low sample volumes in a short time. The developed platform can contribute to the modern clinical diagnostics assays as a miniaturized, reusable, easy in operation tool, with an option of an autonomous analysis. Due to small dimensions of each individual sensor, many detectors can be integrated on a chip that paves a way towards a new type of miniaturized bio-analytics. Namely, the cytometer measurements format coupled to the smart data treatment opens a route towards the realization of a platform for the rapid *detection* and *recognition* of a broad spectrum of *e.g.* blood-related (**Supporting S20**) and immune system diseases. The task of the software is in the utilization of learning algorithms to train the network for the recognition of *multiple data patterns*, indicating different diseases, and used for the diagnostics of multiple patients. As the data complexity increases dramatically in this case, we envision the evolution of the signal treatment methods, *e.g.* towards deep learning approaches[78].

ASSOCIATED CONTENT

Supporting Information available online: Supporting information contains an overview of datasets of healthy and AML-diagnosed donors, comparison of sensing areas in state-of-the-art impedance cytometry geometries, COMSOL simulations on sensor prototyping and electric field between optimized nanowire structure, electric field behavior in the presence of a particle, 3D Hydrodynamic Focusing Calculations, PBMC detection with various flow rates, electrical Characterization in AC and DC, sensitivity towards several numbers of analytes, settling time of a 10µm particle on the sensor, scatter plot pairing and calculation, coefficients of variation (CV) for various sensing areas, phase shift and reference curve for resistance and capacitance shift, resistance and capacitance changes per particle, FACS analysis on subpopulations of healthy PBMCs and AML-diagnosed PBMCs, PBMC sub-population classification, PBMC detection with various sensing sizes and frequencies, manual analysis of PBMCs of healthy and AML-diagnosed donors, full-length Experiment, probing SiO_2 and PBMC mixture, signal modulation using silica microspheres of several diameters, detection Area calculation, detailed material and methods, code for data analysis.

AUTHOR INFORMATION

Corresponding Author

*E-mail: l.baraban@hzdr.de

Author Contributions

J.S, S.K. conducted experiments and simulations under supervision of L.B and G.C. E.A., M.B., A.F., and M.B. L.G.D. and M.R., J.M.M. and K.S. contributed with biological samples from their institutes. L.B, and G.C oversaw the research in their groups. The manuscript was written by L.B and J.S with input from E.A, L.G.D and M.R, S.K. G.M, developed the software for data analysis. All authors co-wrote the paper and agree to its contents.

Notes

The authors declare no competing financial interest.

ACKNOWLEDGMENT

This work was kindly supported by the Initiative and Networking Fund of the Helmholtz Association of German Research Centers through the International Helmholtz Research School for Nanoelectronic Networks, IHRS NANONET (VH-KO-606), cluster of excellence cfaed (EXC 1056) and DFG funds for project BA 4986/7-1. The authors further thank the MIUR JTC Graphene 2015 (G-IMMUNOMICS project) and the European Union HORIZON 2020 research and innovation program under MSCA RISE 2016 project Carbo-Immap grant. n. 734381. L.G.D was partially supported by the Eleonore Trefftz Program 2016 and the Senior Dresden Fellowship Program 2017 in TU Dresden. LB thanks Dr. D. Makarov (HZDR) for discussions of the manuscript. J.M.M. thanks H. Altmann for peripheral blood isolation.

REFERENCES

1. United Nations, Department of Economic and Social Affairs. Population Division. World Population Prospects: The 2017 Revision, Volume II: Demographic Profiles (ST/ESA/SER.A/400). (2017).
2. Caulfield, B. M. & Donnelly, S. C. What is Connected Health and why will it change your practice? *QJM* **106**, 703–707 (2013).
3. Hollis, C. *et al.* Technological innovations in mental healthcare: harnessing the digital revolution. *Br. J. Psychiatry J. Ment. Sci.* **206**, 263–265 (2015).
4. Gstrein, V. Ideation, social construction and drug policy: A scoping review. *Int. J. Drug Policy* **51**, 75–86 (2018).
5. Fleury, A., Sugar, M. & Chau, T. E-textiles in Clinical Rehabilitation: A Scoping Review. *Electronics* **4**, 173–203 (2015).
6. Oung, Q. *et al.* Technologies for Assessment of Motor Disorders in Parkinson's Disease: A Review. *Sensors* **15**, 21710–21745 (2015).
7. Corish, B. Medical knowledge doubles every few months; how can clinicians keep up?, Elsevier Connect (2018), https://www.elsevier.com/connect/medical-knowledge-doubles-every-few-months-how-can-clinicians-keep-up (date of access: 28.07.2020)
8. IBM: The future of health is cognitive, https://www.ibm.com/downloads/cas/LQZ0O1WM (date of access: 12.12.2017)
9. Ballard, Z. S. *et al.* Computational Sensing Using Low-Cost and Mobile Plasmonic Readers Designed by Machine Learning. *ACS Nano* **11**, 2266–2274 (2017).
10. Mahapatra, N. *et al.* Electrostatic Selectivity of Volatile Organic Compounds Using Electrostatically Formed Nanowire Sensor. *ACS Sens.* **3**, 709–715 (2018).
11. Bakker, E., Qattan, M., Mutti, L., Demonacos, C. & Krstic-Demonacos, M. The role of microenvironment and immunity in drug response in leukemia. *Biochim. Biophys. Acta BBA - Mol. Cell Res.* **1863**, 414–426 (2016).

286 12. Stewart, B. W., Wild, C., International Agency for Research on Cancer & World Health
287 Organization. *World cancer report 2014*. (2014).
288 13. De Kouchkovsky, I. & Abdul-Hay, M. 'Acute myeloid leukemia: a comprehensive review and
289 2016 update'''. *Blood Cancer J.* **6**, e441 (2016).
290 14. Wild, C.P., Weiderpass, E., Stewart B.W. *World cancer report: Cancer Research for Cancer*
291 *Prevention*. IARC Press, Lyon 2003).
292 15. Kahng, J. *et al.* Flow Cytometric White Blood Cell Differential Using CytoDiff is Excellent for
293 Counting Blasts. *Ann. Lab. Med.* **35**, 28–34 (2015).
294 16. Eigl, S. *et al.* Galactomannan testing and Aspergillus PCR in same-day bronchoalveolar lavage
295 and blood samples for diagnosis of invasive aspergillosis. *Med. Mycol.* **55**, 528–534 (2017).
296 17. Morozov, V. A. *et al.* No PERV transmission during a clinical trial of pig islet cell transplantation.
297 *Virus Res.* **227**, 34–40 (2017).
298 18. Saez, B., Walter, M. J. & Graubert, T. A. Splicing factor gene mutations in hematologic
299 malignancies. *Blood* **129**, 1260–1269 (2017).
300 19. Baechler, E. C. *et al.* Interferon-inducible gene expression signature in peripheral blood cells of
301 patients with severe lupus. *Proc. Natl. Acad. Sci. U. S. A.* **100**, 2610–2615 (2003).
302 20. Giordano, A. *et al.* Epithelial-Mesenchymal Transition and Stem Cell Markers in Patients with
303 HER2-Positive Metastatic Breast Cancer. *Mol. Cancer Ther.* **11**, 2526–2534 (2012).
304 21. Marshall, N. A. *et al.* Immunosuppressive regulatory T cells are abundant in the reactive
305 lymphocytes of Hodgkin lymphoma. *Blood* **103**, 1755–1762 (2004).
306 22. Gomes, J. a. S. *et al.* Evidence that Development of Severe Cardiomyopathy in Human Chagas'
307 Disease Is Due to a Th1-Specific Immune Response. *Infect. Immun.* **71**, 1185–1193 (2003).
308 23. Ho, L.-J. *et al.* Infection of Human Dendritic Cells by Dengue Virus Causes Cell Maturation and
309 Cytokine Production. *J. Immunol.* **166**, 1499–1506 (2001).

310 24. Challier, J. C. *et al.* Obesity in Pregnancy Stimulates Macrophage Accumulation and
311 Inflammation in the Placenta. *Placenta* **29**, 274–281 (2008).
312 25. Gold, S. M., Chalifoux, S., Giesser, B. S. & Voskuhl, R. R. Immune modulation and increased
313 neurotrophic factor production in multiple sclerosis patients treated with testosterone. *J.*
314 *Neuroinflammation* **5**, 32 (2008).
315 26. Strese, S. *et al.* In vitro and in vivo anti-leukemic activity of the peptidase-potentiated alkylator
316 melflufen in acute myeloid leukemia. *Oncotarget* **8**, 6341–6352 (2017).
317 27. Adan, A., Alizada, G., Kiraz, Y., Baran, Y. & Nalbant, A. Flow cytometry: basic principles and
318 applications. *Crit. Rev. Biotechnol.* **37**, 163–176 (2017).
319 28. Health & Personal Care Costs and Prices Paid - CostHelper.com.
320 https://health.costhelper.com/blood-test.html (Date of access: 23.12.2019).
321 29. Arcizet, O. *et al.* High-sensitivity optical monitoring of a micromechanical resonator with a
322 quantum-limited optomechanical sensor. *Phys. Rev. Lett.* **97**, 133601 (2006).
323 30. Boisen, A., Dohn, S., Keller, S. S., Schmid, S. & Tenje, M. Cantilever-like micromechanical
324 sensors. *Rep. Prog. Phys.* **74**, 036101 (2011).
325 31. Schütt, J. *et al.* Compact Nanowire Sensors Probe Microdroplets. *Nano Lett.* **16** (8), 4991-5000
326 (2016).
327 32. Ibarlucea, B. *et al.* Nanowire sensors monitor bacterial growth kinetics and response to antibiotics.
328 *Lab. Chip* **17**, 4283–4293 (2017).
329 33. Ibarlucea, B. *et al.* Ultrasensitive detection of Ebola matrix protein in a memristor mode. *Nano*
330 *Res.* **11**, 1057–1068 (2018).
331 34. Cui, Y. Nanowire Nanosensors for Highly Sensitive and Selective Detection of Biological and
332 Chemical Species. *Science* **293**, 1289–1292 (2001).
333 35. Zhang, A. & Lieber, C. M. Nano-Bioelectronics. *Chem. Rev.* **116**, 215–257 (2016).

334 36. Kim, D. M.; Jeong, Y.-H. *Nanowire Field Effect Transistors: Principles and Applications,*
335 Springer New York, 2014.
336 37. Jeon, D.-J. et al. Scaling and graphical transport-map analysis of ambipolar Schottky-barrier thin-
337 film transistors based on a parallel array of Si nanowires. Nano Lett.. 15 (7), 4578-4584 (2015).
338 38. Baek, E. *et al.* Negative photoconductance in heavily doped Si nanowire field-effect transistors.
339 *Nano Lett.* **17** (11), 6727-6734 (2017).
340 39. Dastider, S. G., Barizuddin, S., Dweik, M. & Almasri, M. A micromachined impedance biosensor
341 for accurate and rapid detection of E. coli O157:H7. *RSC Adv.* **3**, 26297 (2013).
342 40. Zou, Z., Kai, J., Rust, M. J., Han, J. & Ahn, C. H. Functionalized nano interdigitated electrodes
343 arrays on polymer with integrated microfluidics for direct bio-affinity sensing using impedimetric
344 measurement. *Sens. Actuators Phys.* **136**, 518–526 (2007).
345 41. Muñoz-Berbel, X., Vigués, N., Mas, J., Jenkins, A. T. A. & Muñoz, F. J. Impedimetric
346 characterization of the changes produced in the electrode–solution interface by bacterial attachment.
347 *Electrochem. Commun.* **9**, 2654–2660 (2007).
348 42. Gomez-Sjoberg, R., Morisette, D. T. & Bashir, R. Impedance microbiology-on-a-chip:
349 microfluidic bioprocessor for rapid detection of bacterial metabolism. *J. Microelectromechanical Syst.*
350 **14**, 829–838 (2005).
351 43. Peretz-Soroka, H. *et al.* Optically-Gated Self-Calibrating Nanosensors: Monitoring pH and
352 Metabolic Activity of Living Cells. *Nano Lett.* **13**, 3157–3168 (2013).
353 44. Saleh, O. A. & Sohn, L. L. Quantitative sensing of nanoscale colloids using a microchip Coulter
354 counter. *Rev. Sci. Instrum.* **72**, 4449–4451 (2001).
355 45. Wood, D. K., Oh, S.-H., Lee, S.-H., Soh, H. T. & Cleland, A. N. High-bandwidth radio frequency
356 Coulter counter. *Appl. Phys. Lett.* **87**, 184106 (2005).

357 46. Morgan, H., Holmes, D. & Green, N. G. High speed simultaneous single particle impedance and
358 fluorescence analysis on a chip. *Curr. Appl. Phys.* **6**, 367–370 (2006).
359 47. Schmid, Y. R. F., Bürgel, S. C., Misun, P. M., Hierlemann, A. & Frey, O. Electrical Impedance
360 Spectroscopy for Microtissue Spheroid Analysis in Hanging-Drop Networks. *ACS Sens.* **1**, 1028–1035
361 (2016).
362 48. Larsen, U. D., Blankenstein, G. & Branebjerg, J. Microchip Coulter particle counter. in *Solid State*
363 *Sensors and Actuators, 1997. TRANSDUCERS'97 Chicago., 1997 International Conference on* vol. 2
364 1319–1322 (IEEE, 1997).
365 49. Cheung, K., Gawad, S. & Renaud, P. Impedance spectroscopy flow cytometry: On-chip label-free
366 cell differentiation. *Cytometry A* **65A**, 124–132 (2005).
367 50. Gawad, S., Schild, L. & Renaud, P. Micromachined impedance spectroscopy flow cytometer for
368 cell analysis and particle sizing. *Lab. Chip* **1**, 76–82 (2001).
369 51. Rollo, E. *et al.* Label-free identification of activated T lymphocytes through tridimensional
370 microsensors on chip. *Biosens. Bioelectron.* **94**, 193–199 (2017).
371 52. Heidmann, I., Schade-Kampmann, G., Lambalk, J., Ottiger, M. & Di Berardino, M. Impedance
372 Flow Cytometry: A Novel Technique in Pollen Analysis. *PLOS ONE* **11**, e0165531 (2016).
373 53. McGrath, J. S. *et al.* Analysis of Parasitic Protozoa at the Single-cell Level using Microfluidic
374 Impedance Cytometry. *Sci. Rep.* **7**, 2601 (2017).
375 54. Patolsky, F. & Lieber, C. M. Nanowire nanosensors. *Mater. Today* **8**, 20–28 (2005).
376 55. Bernabini, C., Holmes, D. & Morgan, H. Micro-impedance cytometry for detection and analysis
377 of micron-sized particles and bacteria. *Lab. Chip* **11**, 407–412 (2011).
378 56. Berkel, C. van *et al.* Integrated systems for rapid point of care (PoC) blood cell analysis. *Lab. Chip*
379 **11**, 1249–1255 (2011).

380 57. Barat, D., Spencer, D., Benazzi, G., Mowlem, M. C. & Morgan, H. Simultaneous high speed
381 optical and impedance analysis of single particles with a microfluidic cytometer. *Lab. Chip* **12**, 118–
382 126 (2012).
383 58. Hassan, U., Watkins, N. N., Edwards, C. & Bashir, R. Flow metering characterization within an
384 electrical cell counting microfluidic device. *Lab. Chip* **14**, 1469–1476 (2014).
385 59. Simon, P., Frankowski, M., Bock, N. & Neukammer, J. Label-free whole blood cell differentiation
386 based on multiple frequency AC impedance and light scattering analysis in a micro flow cytometer.
387 *Lab. Chip* **16**, 2326–2338 (2016).
388 60. Carbonaro, A., Godley, L. A. & Sohn, L. L. The NanoCytometer: Screening Cells Based on Cell
389 Size. in *2006 International Conference on Microtechnologies in Medicine and Biology* 206–208
390 (2006). doi:10.1109/MMB.2006.251529.
391 61. Nerowski, A., Opitz, J., Baraban, L. & Cuniberti, G. Bottom-up synthesis of ultrathin straight
392 platinum nanowires: Electric field impact. *Nano Res.* **6**, 303–311 (2013).
393 62. Sun, T. & Morgan, H. Single-cell microfluidic impedance cytometry: a review. *Microfluid.*
394 *Nanofluidics* **8**, 423–443 (2010).
395 63. Kleiveland, C. R. Peripheral Blood Mononuclear Cells. in *The Impact of Food Bioactives on*
396 *Health* 161–167 (Springer, Cham, 2015). doi:10.1007/978-3-319-16104-4_15.
397 64. Holmes, D. *et al.* Leukocyte analysis and differentiation using high speed microfluidic single cell
398 impedance cytometry. *Lab. Chip* **9**, 2881–2889 (2009).
399 65. Holmes, D. & Webb, B. L. J. Electrical Impedance Cytometry. in *Encyclopedia of*
400 *Nanotechnology* (ed. Bhushan, B.) 662–671 (Springer Netherlands, 2012). doi:10.1007/978-90-481-
401 9751-4_122.

402 66. Polevaya, Y., Ermolina, I., Schlesinger, M., Ginzburg, B.-Z. & Feldman, Y. Time domain
403 dielectric spectroscopy study of human cells: II. Normal and malignant white blood cells. *Biochim.*
404 *Biophys. Acta BBA - Biomembr.* **1419**, 257–271 (1999).
405 67. Yang, J. *et al.* Dielectric properties of human leukocyte subpopulations determined by
406 electrorotation as a cell separation criterion. *Biophys. J.* **76**, 3307–3314 (1999).
407 68. Polliack, A. *Normal, Transformed and Leukemic Leukocytes: A Scanning Electron Microscopy*
408 *Atlas*. (Springer Science & Business Media, 2012).
409 69. Wang, X.-B. *et al.* Changes in Friend murine erythroleukaemia cell membranes during induced
410 differentiation determined by electrorotation. *Biochim. Biophys. Acta BBA - Biomembr.* **1193**, 330–344
411 (1994).
412 70. Gascoyne, P. R. C., Shim, S., Noshari, J., Becker, F. F. & Stemke-Hale, K. Correlations between
413 the Dielectric Properties and Exterior Morphology of Cells Revealed by Dielectrophoretic Field-Flow
414 Fractionation. *Electrophoresis* **34**, 1042–1050 (2013).
415 71. Russier, J. *et al.* Few-Layer Graphene Kills Selectively Tumor Cells from Myelomonocytic
416 Leukemia Patients. *Angew. Chem.-Int. Ed.* **56**, 3014–3019 (2017).
417 72. Orecchioni, M. *et al.* Single-cell mass cytometry and transcriptome profiling reveal the impact of
418 graphene on human immune cells. *Nat. Commun.* **8**, 1109 (2017).
419 73. Liu, F. T., Ting, K. M. & Zhou, Z.-H. Isolation-Based Anomaly Detection. *Acm Trans. Knowl.*
420 *Discov. Data* **6**, 3 (2012).
421 74. Lloyd, S. Least-Squares Quantization in Pcm. *Ieee Trans. Inf. Theory* **28**, 129–137 (1982).
422 75. Vardiman, J. W., Harris, N. L. & Brunning, R. D. The World Health Organization (WHO)
423 classification of the myeloid neoplasms. *Blood* **100**, 2292–2302 (2002).

424 76. Foster, M. C. *et al.* Detection of Measurable Residual Disease (MRD) in Peripheral Blood: First
425 Report of a Novel Microfluidic Platform in Patients with Acute Myeloid Leukemia (AML). *Blood* **134**,
426 1417–1417 (2019).
427 77. Zeijlemaker, W. *et al.* Peripheral blood minimal residual disease may replace bone marrow
428 minimal residual disease as an immunophenotypic biomarker for impending relapse in acute myeloid
429 leukemia. *Leukemia* **30**, 708–715 (2016).
430 78. Wang, J., Chen, Y., Hao, S., Peng, X. & Hu, L. Deep Learning for Sensor-based Activity
431 Recognition: A Survey. *Pattern Recognit. Lett.* **119**, 3-11 (2018).
432 79. Winer, M. H., Ahmadi, A. & Cheung, K. C. Application of a three-dimensional (3D) particle
433 tracking method to microfluidic particle focusing. *Lab Chip* **14**, 1443–1451 (2014).
434 80. Shoemark, A. *et al.* Accuracy of Immunofluorescence in the Diagnosis of Primary Ciliary
435 Dyskinesia. *Am. J. Respir. Crit. Care Med.* **196**, 94–101 (2017).
436 81. Rinke, C. *et al.* Obtaining genomes from uncultivated environmental microorganisms using
437 FACS–based single-cell genomics. *Nat. Protoc.* **9**, 1038–1048 (2014).

438

439

440

Figures

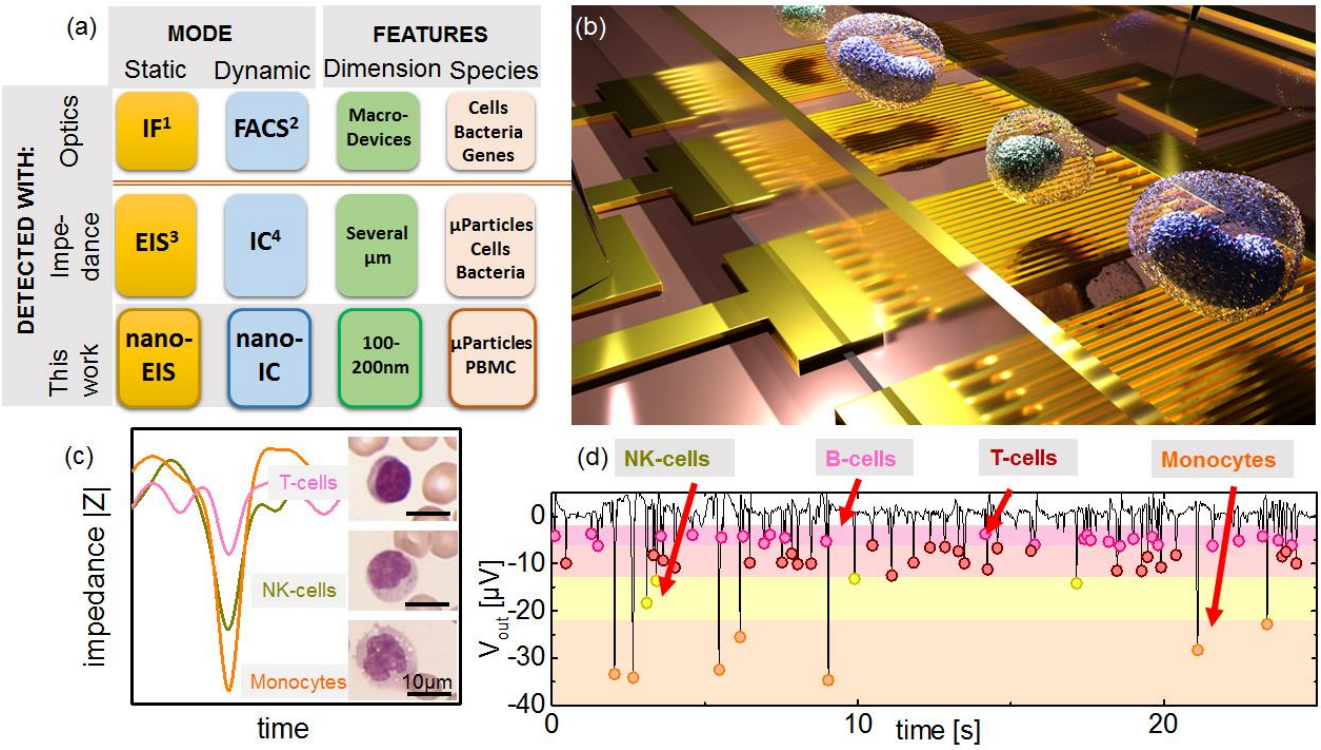

Figure 1: Conceptual figure describing the developed sensor platform. **(a)** Contribution of the nano-sensor platform to previously reported and state of the art techniques, *i.e.* immunofluorescence (IF)[80], fluorescence-activated cell sorting (FACS)[81], electrical impedance spectroscopy (EIS)[47] and impedance cytometry (IC)[64]. **(b)** Schematically illustration of PBMC detection by nano-impedance cytometry **(c)** Comparison of signal magnitudes of PBMCs with different diameters. **(d)** Real-time output response of the sensor with complex mixture of PBMCs.

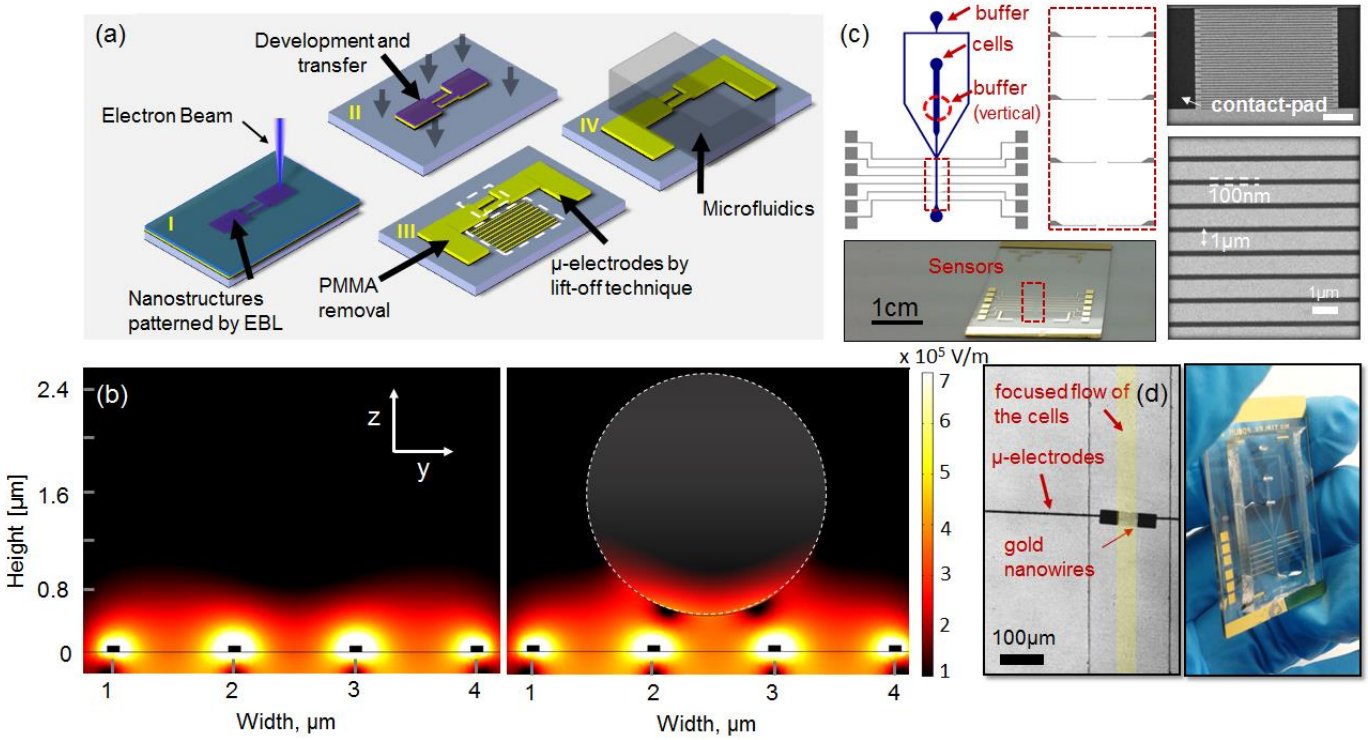

Figure 2: Fabrication and integration of the nanoscaled sensor chip. (**a**) Nano-impedance cytometer fabrication process. (**b**) COMSOL Multiphysics simulation of the electric field perturbation in presence of a dielectric microparticle in the microfluidic channel. (**c**) Layout of the nano-sensor array of 6 independent accessible electrode pairs approaching the contact pads of the EBL-patterned design. The main channel of the microfluidic geometry is placed to incorporate the electrodes. (**d**) 3D hydrodynamic focusing technique allowing analyte guidance in the middle and at the bottom of the channel.

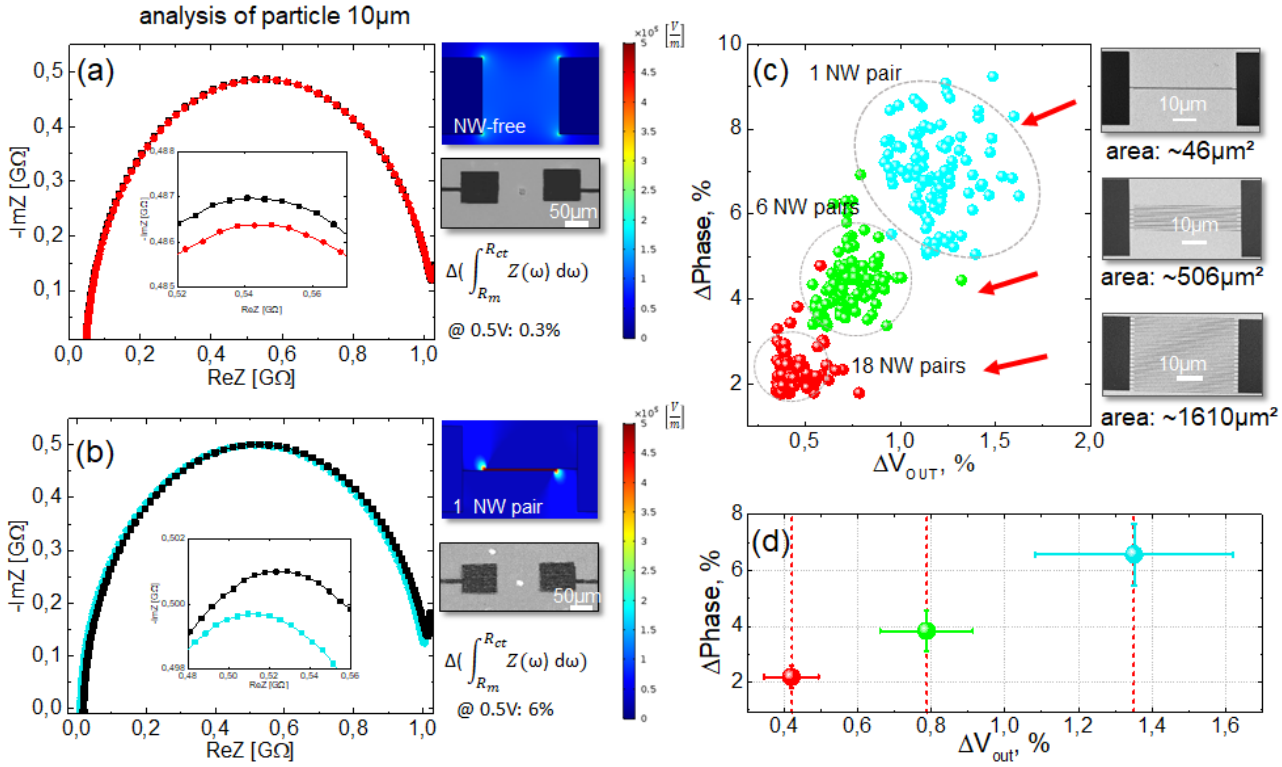

Figure 3: Comparison of the signal change with and w/o present micro-particle in the sensing area in static mode. While **(a)** only micro-electrodes grant a weak electric field and thus have a small signal change when a particle is present (0.26%), introduction of 16 interdigitating nanowires **(b)** and single nanowire pair. **(c)** cytometer mode summary: signal modulation while detecting 10 µm particle, using different sensor dimensions. **(d)** Calculated change of device output signal in dependence of sensor dimensions, from **(c)**.

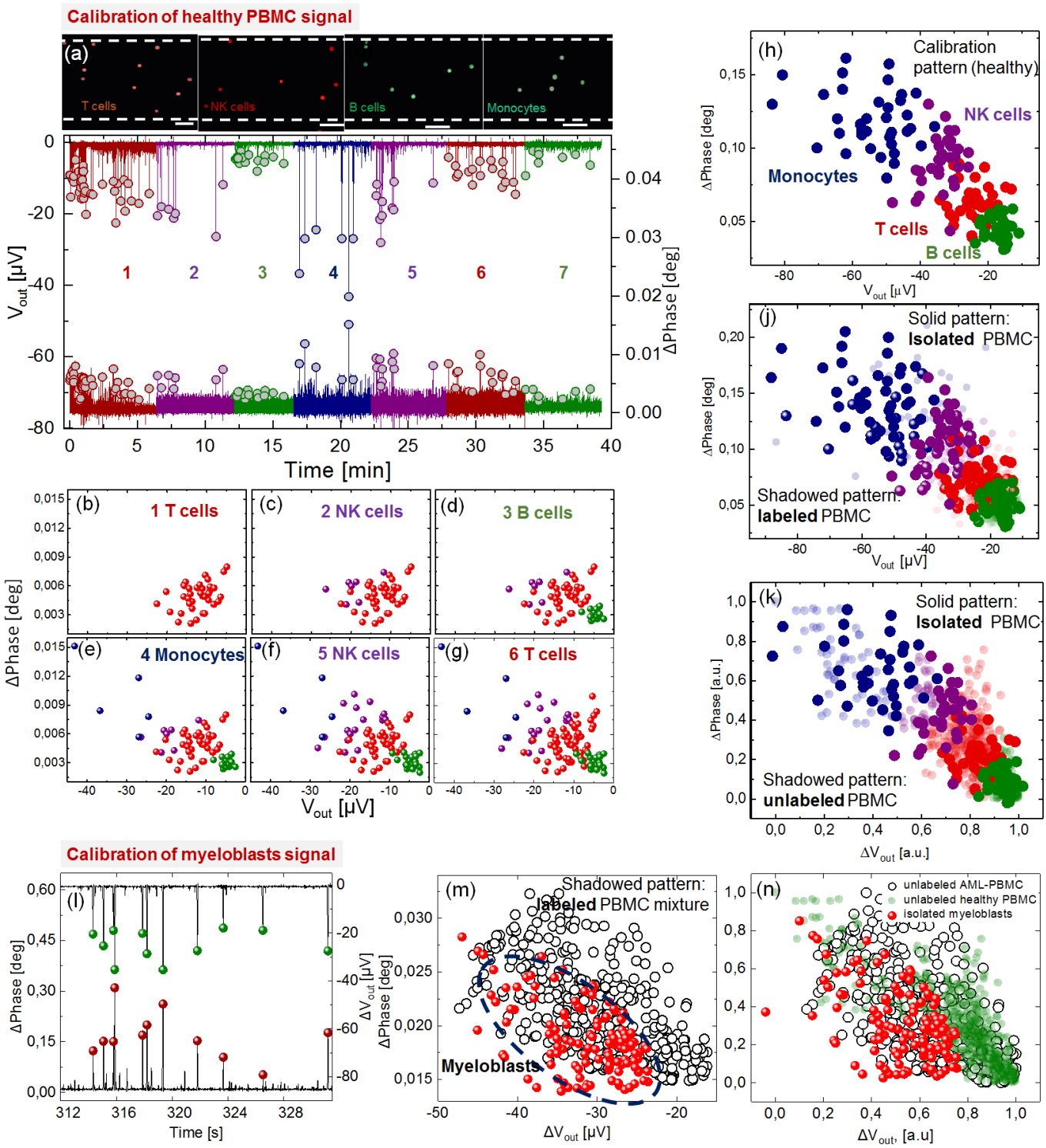

Figure 4: Detection and classification of isolated PBMCs and formation of the calibration pattern. **(a)** detection of the main subpopulations of PBMCs one-by-one, *i.e.* lymphocytes and monocytes. (b-g) Formation of the pattern: plot of individually measured fluorescently labelled PBMC cells. **(h)** Exemplary calibration pattern. **(j)** Impedance cytometry of unlabeled PBMCs: matching of the labelled PBMC mixture with the calibration pattern. The lymphocyte cluster is divided based on its subpopulations, namely NK-, T-, and B-cells. (**k**) Matching the

unlabelled PBMC mixture with the calibration pattern. The lymphocyte cluster is divided based on its subpopulations, namely NK-, T-, and B-cells. Panels (l)-(n): calibration of the signal for impedimetric detection of myeloblasts. (l) Detection of the labeled isolated blasts one-by-one in time domain; (m) formation of the data cloud and its localization within the pattern of peripheral blood of the AML positive donor; (n) matching the myeloblasts cluster (red) with the unlabeled PBMC of the AML positive donor (black open circles) and PBMC of healthy donor (gray circles).

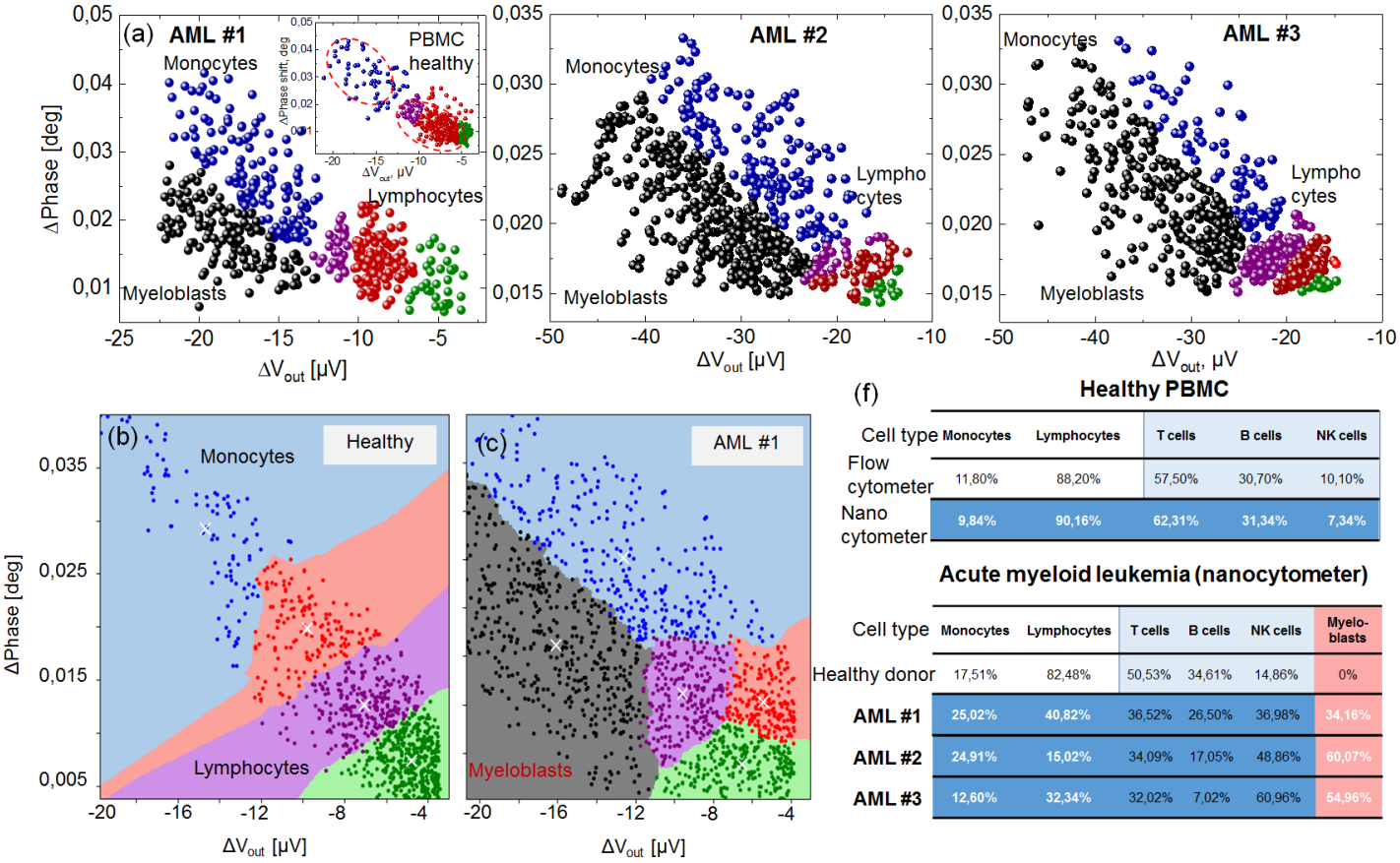

(f)

Healthy PBMC

Cell type	Monocytes	Lymphocytes	T cells	B cells	NK cells
Flow cytometer	11,80%	88,20%	57,50%	30,70%	10,10%
Nano cytometer	9,84%	90,16%	62,31%	31,34%	7,34%

Acute myeloid leukemia (nanocytometer)

Cell type	Monocytes	Lymphocytes	T cells	B cells	NK cells	Myelo-blasts
Healthy donor	17,51%	82,48%	50,53%	34,61%	14,86%	0%
AML #1	25,02%	40,82%	36,52%	26,50%	36,98%	34,16%
AML #2	24,91%	15,02%	34,09%	17,05%	48,86%	60,07%
AML #3	12,60%	32,34%	32,02%	7,02%	60,96%	54,96%

Figure 5: (a) Detection and characterization of PBMC of healthy human donors (see Inset) and AML patients#1-3. A new cluster is found in the AML samples caused by the presence of the myeloblast subfamily. (**b**) Impedance cytometry scatter plot of PBMCs of healthy donor (n=1000 cells) and **(c)** AML patient (n=1400 cells) calculated via the machine learning algorithm. **(d)** Overview of the individual cell counts, comparison to healthy patient. AML patients PBMCs shows a myeloblast percentage in the range 30-60%.

TOC image:

Ultra-compact nanocytometer for real-time impedimetric detection and classification of subpopulations of living cells in peripheral blood.